Non-zonal detached eddy simulation coupled with a steady RANS solver in the wall region

International Journal of Heat and Fluid Flow 92 (2021) 108880

Contents lists available at ScienceDirect

International Journal of Heat and Fluid Flow

journal homepage: www.elsevier.com/locate/ijhff

Non-zonal detached eddy simulation coupled with a steady RANS solver in the wall region

L. Davidson

Division of Fluid Dynamics, Department of Mechanics and Maritime Sciences, Chalmers University of Technology, SE-412 96 Gothenburg, Sweden

ARTICLE INFO

Keywords:
DES
Hybrid LES-RANS
Dual mesh

ABSTRACT

Xiao and Jenny (2012) proposed an interesting hybrid LES/RANS method in which they use two solvers and solve the RANS and LES equations in the entire computational domain. In the present work this method is simplified and used as a hybrid RANS-LES method, a *wall-modeled* LES. The two solvers are employed in the entire domain. Near the walls, the flow is governed by the steady RANS solver; drift terms are added to the DES equations to ensure that the time-averaged DES fields agree with the steady RANS field. Away from the walls, the flow is governed by the DES solver; in this region, the RANS field is set to the time-averaged LES field. The disadvantage of traditional DES models is that the RANS models in the near-wall region – which originally were developed and tuned for steady RANS – are used as URANS models where a large part of the turbulence is resolved. In the present method – where steady RANS is used in the near-wall region – the RANS turbulence models are used in a context for which they were developed. In standard DES methods, the near-wall accuracy can be degraded by the unsteady agitation coming from the LES region. It may in the present method be worth while to use an accurate, advanced RANS model. The EARSM model is used in the steady RANS solver. The new method is called **NZ S-DES**. It is found to substantially improve the predicting capability of the standard DES. A great advantage of the new model is that it is insensitive to the location of the RANS-LES interface.

1. Introduction

DES (Detached-Eddy Simulation) uses unsteady RANS near walls (URANS region) and LES further away from walls (LES region). The resolved turbulence in the URANS region is often larger than the modeled part. But the RANS models used in the URANS region were originally developed and tuned in steady RANS simulations. Hence the accuracy and the validity of the RANS models in the URANS region can be questioned. In the present work, DES is coupled with *steady* RANS near the walls. We denote the method NZ S-DES (Non-Zonal approach using Steady RANS coupled to DES).

Xiao and Jenny (2012) proposed a new method in which they solve both the LES and RANS equations in the entire domain. The flow is in the near-wall region governed by the RANS equations and in the outer region it is governed by the LES equations. This is achieved by adding drift terms in the LES and RANS equations. In the interface region(s), the drift terms are modified by a linear ramp function. Drift terms are used in all equations in the RANS equations (momentum equations, the pressure equation (PISO is used)) and in the modeled turbulent equations (k and ε). Two drift terms are added in the LES momentum equations; one to ensure that the mean velocity fields in the RANS and LES equations are the same and one to ensure that the total turbulent kinetic energies are the same.

In Xiao et al. (2013) they extended the method to account for non-conformal meshes. They used a Cartesian mesh for the LES equations and a body-fitted mesh for the RANS equations. They applied the method to fully developed channel flow and the flow over periodic hills. The paper shows how an accurate academic solver – massively parallel – can be combined with industrial, flexible RANS solvers.

Tunstall et al. (2017) implemented the method in Xiao and Jenny (2012) and modified it (different ramp function, different constants, reducing the number of case-specific constants etc.). They applied it to fully developed channel flow and a rather complex flow consisting of a pipe junction including heat transfer. Hence, they had to introduce drift terms also in the energy equations.

de Laage de Meux et al. (2015) used forcing to achieve resolved Reynolds stress profiles equal to target modeled RANS stress profiles. The resolved Reynolds stresses were averaged in time in the same way as in Xiao and Jenny (2012), Tunstall et al. (2017).

Breuer and Schmidt (2014) used an advanced RANS turbulence model – the Explicit Algebraic Reynolds Stress Model, EARSM – in an hybrid LES-RANS methodology. However, as mentioned above, the disadvantage is that the RANS equations were solved in transient mode, where a large part of the large-scale turbulence is resolved.

E-mail address: lars.davidson@chalmers.se.

https://doi.org/10.1016/j.ijheatfluidflow.2021.108880
Received 1 April 2021; Received in revised form 19 August 2021; Accepted 9 October 2021
Available online 1 November 2021

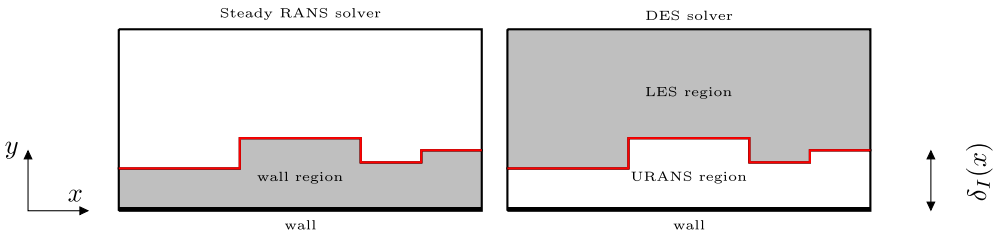

(a) Steady RANS solver (b) DES solver

Fig. 1. Gray color indicates the solver that drives the flow. The interface, I, is shown in red. (For interpretation of the references to color in this figure legend, the reader is referred to the web version of this article.)

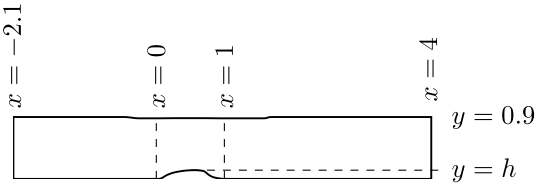

Fig. 2. The domain of the hump.

Davidson (2019a) used the same model as in the present study. In Davidson (2019a), however, the interface was defined along a pre-selected gridline and the grid in the hump flow simulations was much coarser upstream the hump and in the outlet region than in the present work. Moreover, the present work uses a different timescale in the drift term as well as evaluates different SGS length scales (Δ_{DES} and Δ_{IDDES}, see Eq. (12)).

Recently, in Nguyen et al. (2020) they presented an interesting dual-mesh approach where they used the method in Schumann (1975) of expressing the SGS stress tensor in S_{ij} (instantaneous) and $\langle S_{ij}\rangle$ (time-averaged). In Nguyen et al. (2020) they formulated the SGS stress tensor as a blend, taking S_{ij} from the LES solver and $\langle S_{ij}\rangle$ from the RANS solver, i.e.

$$\tau_{ij} - \tau_{kk}\delta_{ij} = -2f_b\nu_{t,LES}\left(S_{ij} - \langle S_{ij}\rangle\right) - 2(1-f_b)\nu_{t,RANS}S_{ij}$$

In the present study, the steady RANS equations are solved. Here it makes sense to use advanced RANS turbulence models, since these models were developed for steady RANS. The EARSM (Wallin and Johansson, 2000) is used in the RANS solver. The present method is in many aspects similar to that proposed in Xiao and Jenny (2012), Tunstall et al. (2017) but it is simplified: the RANS equations are used in steady mode, a more advanced RANS turbulence model is used and the present method includes fewer drift terms and tuning constants.

2. Numerical solvers

The momentum equations with an added turbulent viscosity read

$$\frac{\partial \bar{u}_i}{\partial t} + \frac{\partial \bar{u}_j\bar{u}_i}{\partial x_j} = \delta_{1i} - \frac{1}{\rho}\frac{\partial \bar{p}}{\partial x_i} + \frac{\partial}{\partial x_j}\left(\left(\nu + \nu_t\right)\frac{\partial \bar{u}_i}{\partial x_j}\right) \tag{1}$$

where the first term on the right side is the driving pressure gradient in the streamwise direction, which is used in the fully-developed channel flow simulations. The overbar, $\bar{\cdot}$, denotes volume filtering in the LES region and short-time filtering in the URANS region; for the RANS solver it denotes the usual RANS averaging. The velocities, pressure etc. are time averaged when presenting the results below which is denoted by angular brackets, $\langle\cdot\rangle$. The decomposition is defined as $\bar{v}_i = \langle\bar{v}_i\rangle + \bar{v}_i'$ where $\bar{v}_i'$ denotes a URANS or LES (i.e. a DES) fluctuation.

2.1. DES solver

An incompressible, finite volume code is used (Davidson and Peng, 2003a; Davidson, 2018). The convective terms in the momentum equations are discretized using central differencing. Hybrid central/upwind is used for the k and ω equations. The Crank–Nicolson scheme is used for time discretization of all equations. The numerical procedure is based on an implicit, fractional step technique with a multigrid pressure Poisson solver (Emvin, 1997) and a non-staggered grid arrangement.

The discretized momentum equations read

$$\bar{u}_i^{n+1/2} = \bar{u}_i^n + \Delta t H\left(\bar{u}^n, \bar{u}_i^{n+1/2}\right) - \alpha\Delta t\frac{\partial \bar{p}^{n+1/2}}{\partial x_i} - (1-\alpha)\Delta t\frac{\partial \bar{p}^n}{\partial x_i} \tag{2}$$

where H includes convective, viscous and SGS terms. In SIMPLE notation (Patankar, 1980) this equation reads

$$a_P\bar{u}_i^{n+1/2} = \sum_{nb} a_{nb}\bar{u}^{n+1/2} + S_U - \alpha\Delta t\frac{\partial \bar{p}^{n+1/2}}{\partial x_i}\Delta V$$

where S_U includes all source terms except the implicit pressure; $\alpha = 0.5$ in channel flow and boundary-layer flow (Crank–Nicolson) and $\alpha = 1$ (fully implicit) in the hump flow. The face velocities $\bar{u}_{f,i}^{n+1/2} = 0.5(\bar{u}_{i,j}^{n+1/2} + \bar{u}_{i,j-1}^{n+1/2})$ (note that j denotes node number and i is a tensor index) do not satisfy continuity. Create an intermediate velocity field by subtracting the implicit pressure gradient from Eq. (2), i.e.

$$\bar{u}_i^* = \bar{u}_i^n + \Delta t H\left(\bar{u}^n, \bar{u}_i^{n+1/2}\right) - (1-\alpha)\Delta t\frac{\partial \bar{p}^n}{\partial x_i} \tag{3a}$$

$$\Rightarrow \bar{u}_i^* = \bar{u}_i^{n+1/2} + \alpha\Delta t\frac{\partial \bar{p}^{n+1/2}}{\partial x_i} \tag{3b}$$

Take the divergence of Eq. (3b) and require that $\partial\bar{u}_{f,i}^{n+1/2}/\partial x_i = 0$ so that

$$\frac{\partial^2 \bar{p}^{n+1}}{\partial x_i \partial x_i} = \frac{1}{\Delta t\alpha}\frac{\partial \bar{u}_{f,i}^*}{\partial x_i} \tag{4}$$

The Poisson equation for $\bar{p}^{n+1}$ is solved with an efficient multigrid method (Emvin, 1997). In the 3D MG we use a plane-by-plane 2D MG. After that, the face velocities are corrected as

$$\bar{u}_{f,i}^{n+1} = \bar{u}_{f,i}^* - \alpha\Delta t\frac{\partial \bar{p}^{n+1}}{\partial x_i} \tag{5}$$

1. Solve the discretized filtered Navier–Stokes equation, Eq. (3a), for $\bar{u}_1$, $\bar{u}_2$ and $\bar{u}_3$.
2. Create an intermediate velocity field $\bar{u}_i^*$ from Eq. (3b).
3. Use linear interpolation to obtain the intermediate velocity field, $\bar{u}_{f,i}$, at the face
4. The Poisson equation (Eq. (4)) is solved with an efficient multigrid method (Emvin, 1997).
5. Compute the face velocities (which satisfy continuity) from the pressure and the intermediate face velocity from Eq. (5)
6. The k and ω equations are solved.

7. The turbulent viscosity is computed.
8. Step 1 to 7 are performed till convergence (usually two iterations) is reached.
9. Next time step.

More details can be found in Davidson and Peng (2003b).

2.2. RANS solver

An incompressible, finite volume code – CALC-BFC (Davidson and Farhanieh, 1995) – is used. The transient term in Eq. (1) (the first term on the left side) is not included. The convective terms in the momentum equations are discretized using the second-order bounded scheme, MUSCL (van Leer, 1979). Hybrid central/upwind is used for the k and ω equations. The numerical procedure is based on pressure-correction method, SIMPLEC, and a staggered grid arrangement.

3. The NZ S-DES methodology

Two sets of equations are solved (steady RANS solver, see Fig. 1(a) and DES solver, see Fig. 1(b)) in the entire domain on identical grids. The steady RANS solver may be two dimensional (as in the present work). The location of the interface *in* the DES solver is defined in the same way as *between* the RANS solver and the DES solver. Drift terms are added in the DES equations, S_i^{DES}, in the URANS region, see Fig. 1. The drift terms in the DES velocity equations read

$$S_i^{DES} = \frac{\langle \bar{v}_i^{RANS} \rangle_T - \langle \bar{v}_i^{DES} \rangle_T}{\tau_r} \tag{6}$$

where

$$\tau_r = \max(C_r/(C_\mu \omega), \Delta t), \quad C_r = 0.1 \tag{7}$$

following Tunstall et al. (2017). No drift term is used in the pressure equation. $\langle \cdot \rangle_T$ indicates a time average over time, T, i.e.

$$\begin{aligned} &\langle \phi(t) \rangle_T = \frac{1}{T} \int_{-\infty}^{t} \phi(\tau) \exp(-(t-\tau)/T) d\tau \Rightarrow \\ &\langle \phi \rangle_T^{n+1} \equiv \langle \phi \rangle_T = a \langle \phi \rangle_T^n + (1-a)\phi^n, \end{aligned} \tag{8}$$

where $a = 1/(1 + \Delta t/T)$ and n denotes the timestep number. It is a method of approximating the time average which can be expressed as a differential form which can be discretized (second line) (Meneveau et al., 1996). Note that although the flow cases in the present work include homogeneous direction(s), no space averaging is made in Eq. (8). It may be noted that although the velocity field in the RANS solver is steady, it is time averaged when used in Eqs. (6) and (9) because it varies slightly in time. This time averaging is probably not necessary.

In the LES region, see Fig. 1, the RANS velocities are prescribed as $\bar{v}_i^{RANS} = \langle \bar{v}_i^{LES} \rangle_T$ by adding a large source term, i.e.

$$\begin{aligned} S_i^{RANS} &= \frac{\langle \bar{v}_i^{LES} \rangle_T - \langle \bar{v}_i^{RANS} \rangle_T}{\epsilon} \\ \bar{p}^{RANS} &= \langle \bar{p}^{LES} \rangle_T \end{aligned} \tag{9}$$

where $\epsilon = 10^{-10}$. The pressure correction is set to zero. This means that, in reality, the steady RANS solver needs to be solved only in the URANS region. In the LES region, the momentum equations in the RANS solver are merely transporting the turbulence quantities, k and ω, to ensure that correct values of k and ω are transported into the URANS region through the RANS-LES interface at $y = \delta_I$, see Fig. 1.

Since the RANS pressure and the velocity field in the LES region are given by the LES flowfield (Eq. (9)), the pressure and the streamwise velocity adjacent to the RANS-LES interface, $\langle \bar{p}_{j+1}^{LES} \rangle_T$ and $\langle \bar{u}_{j+1}^{LES} \rangle_T$, respectively, act as a boundary condition for the RANS equations in the URANS region, see Fig. 3. The wall-normal velocity, $\bar{v}_j^{RANS}$, is solved for using the pressure at node $j+1$. The RANS solver is called every 10th time step.

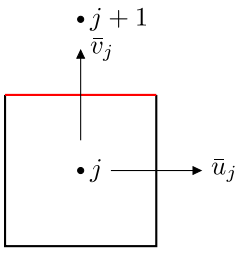

Fig. 3. Control volume, j, in the URANS region (RANS solver) adjacent to the interface, I (in red). (For interpretation of the references to color in this figure legend, the reader is referred to the web version of this article.)

3.1. The $k-\omega$ DES model

The Wilcox $k-\omega$ turbulence DES model reads

$$\begin{aligned} \frac{dk}{dt} &= P^k + \frac{\partial}{\partial x_j}\left[\left(\nu + \frac{\nu_t}{\sigma_k}\right)\frac{\partial k}{\partial x_j}\right] - F_{DES} C_\mu k\omega \\ \frac{d\omega}{dt} &= C_{\omega_1}\frac{\omega}{k}P^k - C_{\omega 2}\omega^2 + \frac{\partial}{\partial x_j}\left[\left(\nu + \frac{\nu_t}{\sigma_\omega}\right)\frac{\partial \omega}{\partial x_j}\right] \\ \nu_t &= \frac{k}{\omega} \end{aligned} \tag{10}$$

where $d/dt = \partial/\partial t + \bar{v}_j \partial/\partial x_j$ ($\partial/\partial t = 0$ in the RANS solver). The standard coefficients are used, i.e. $C_{\omega 1} = 5/9$, $C_{\omega 2} = 3/40$, $\sigma_k = \sigma_\omega = 2$ and $C_\mu = 0.09$. The F_{DES} function is computed as

$$F_{DES} = \max\left\{\frac{L_t}{\Delta}\right\} = \max\left\{\frac{k^{1/2}/(C_\mu \omega)}{\Delta}\right\} \tag{11}$$

Two different options for the LES length scale, Δ, are used, either from DES (Spalart et al., 1997) or IDDES (Shur et al., 2008), i.e.

$$\begin{aligned} \Delta &\equiv \Delta_{DES} = C_{DES}\Delta_{max}, \quad \Delta_{max} = \max\{\Delta x, \Delta y, \Delta z\} \\ \Delta &\equiv \Delta_{IDDES} = C_{IDDES} \min\left(\max\left[C_{dw} d_w, C_w \Delta_{max}, \Delta_{step}\right], \Delta_{max}\right) \\ C_{DES} &= 0.67, \quad C_{IDDES} = 0.7 \end{aligned} \tag{12}$$

where d_w is the wall distance, $C_{dw} = 0.15$, Δ_{step} is the grid cell size in the wall-normal direction.

The DES equations are solved in the entire region, but they govern the flow only in the LES region, see Fig. 1. The location of the interface *in* the DES solver and *between* the RANS solver and the DES solver is defined by Eq. (11).

3.2. The $k-\omega$ EARSM model in the RANS solver

The steady RANS equations are solved in the entire region, but they govern the flow only in the URANS region, see Fig. 1. The $k-\omega$ in Eq. (10) is used with $F_{DES} = 1$ and the transient terms are set to zero. The Reynolds stresses, $\overline{v_i' v_j'}$, are computed from the two-dimensional explicit algebraic Reynolds stress model (EARSM) (Wallin and Johansson, 2000).

3.3. Initialization

The simulations are initialized as follows: first the 2D RANS equations are solved. The initial time averaged fields, $\langle v_i^{LES} \rangle_T$ and $\langle v_i^{RANS} \rangle_T$, are set from the 2D RANS field. Anisotropic synthetic fluctuations, $(\mathcal{V}_i')_m$, are then superimposed to the 2D RANS field which gives the initial DES velocity field.

In order to compute $(\mathcal{V}_i')_m$, synthetic fluctuations, $v_{i,synt}'$, are computed plane-by-plane ($y-z$) in the same way as prescribing inlet boundary conditions, see Section 4.2. They are created by prescribing an integral length scale L_{int}, in the $y-z$ plane. However, there is no correlation between the synthetic fluctuations in adjacent $y-z$ planes.

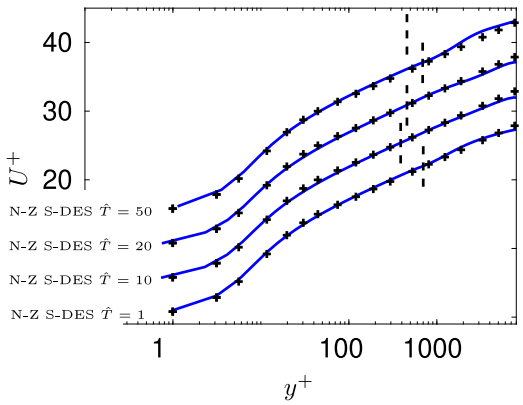

Fig. 4. Channel flow. NZ S-DES. Comparison using different integration time scales, $\hat{T}$. + : Reichardt's law, $U^+ = \frac{1}{\kappa}\ln(1-0.4y^+) + 7.8\left[1-\exp\left(-y^+/11\right) - (y^+/11)\exp\left(-y^+/3\right)\right]$. Vertical thick black lines show RANS-LES interface.

Hence, the synthetic fluctuations in adjacent $y-z$ planes are coupled with an asymmetric space filter

$$(\mathcal{V}_i')_m = a(\mathcal{V}_i')_{m-1} + b(v'_{synt,i})_m \tag{13}$$

where m denotes the index of the x location and $a = \exp(-\Delta x/L_{int})$, $b^2 = 1-a^2$, where Δx and L_{int} denote the grid size and the integral length scale, respectively ($L_{int} = 0.2$).

3.4. NZ S-DES compared to earlier work

- The present method is similar to those in Xiao and Jenny (2012), de Laage de Meux et al. (2015), Tunstall et al. (2017). The main differences are that
  - In Xiao and Jenny (2012), Tunstall et al. (2017) they use one additional drift terms in the LES momentum equations to control resolved Reynolds stresses
  - In Tunstall et al. (2017), the switch between the RANS and DES solver takes place over a number of cells in the wall-normal direction defined by a linear ramp function; in Xiao and Jenny (2012) they use it in the initial part of the simulations in order to stabilize the coupling between the RANS and DES solvers. In the present work the switch takes place abruptly over one cell defined by Eq. (11).
  - They include drift terms in the Poisson equations for the pressure (Eq. (4))
  - They include drift terms also in the k and ε equations (Xiao and Jenny, 2012) or the k equations (Tunstall et al., 2017).
  - In Xiao and Jenny (2012), Tunstall et al. (2017) they include five tuning constants in all drift terms. In the present method, there are two (T and C_r).

4. Results

4.1. Fully-developed channel flow

The first test case is fully developed channel flow with periodic boundary conditions in streamwise (x) and spanwise (z) directions. The Reynolds number, $Re_\tau = u_\tau h/\nu$, is 8000 where h denotes half-channel width. The size of the domain is $x_{max} = 3.2h$, $y_{max} = 2h$ and $z_{max} = 1.6h$ ($h = 1$). The mesh has $32 \times 96 \times 32$ (x, y, z) cells. $\Delta z^+ = 400$ and $\Delta x^+ = 800$. Superscript + denotes that velocities are scaled by the friction velocity, u_τ, and length scales are scaled by the viscous length scale, ν/u_τ so that $y^+ = u_\tau y/\nu$. The timestep is set to $\Delta\hat{t} \equiv \Delta t U_b/h = 0.025$ (U_b denotes bulk velocity) which gives $CFL < 0.4$. It is found that it is important that the sampling time is much larger than the integration time, T (see Eq. (8)). If it is too small, it may give an asymmetric time-averaged flow field. Simulations with different values of $\hat{T}$ are presented in Fig. 4 (for more detail, see Davidson (2019b)). The time, $\mathcal{T}$, to reach fully developed condition and sampling time are both set to $\hat{\mathcal{T}} \equiv \mathcal{T}U_b/h = 1000$ except for $\hat{T} = 50$ for which they are set to $\hat{\mathcal{T}} \equiv \mathcal{T}U_b/h = 2000$. As can be seen, the influence is of $\hat{T}$ on

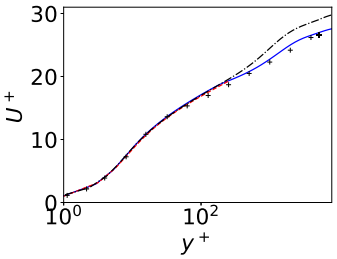

Fig. 5. Channel flow. NZ S-DES compared with standard DES. Δ_{DES} is used (see Eq. (12)). ——: DES solver in NZ S-DES; – –: RANS solver in NZ S-DES; – · –: Standard DES; + : Reichardt's law, $U^+ = \frac{1}{\kappa}\ln(1-0.4y^+) + 7.8\left[1-\exp\left(-y^+/11\right) - (y^+/11)\exp\left(-y^+/3\right)\right]$.

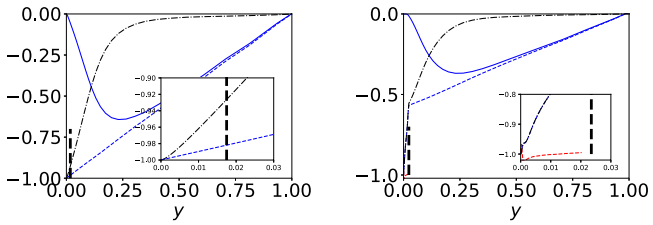

(a) Standard DES. (b) NZ S-DES.

Fig. 6. Channel flow. Shear stresses scaled with u_τ^2. Δ_{DES} is used (see Eq. (12)). Vertical black dashed lines show predicted RANS-LES interface. ——: resolved; – · –: viscous + modeled; – –: total. – –: viscous plus modeled in RANS solver (EARSM) in NZ S-DES.

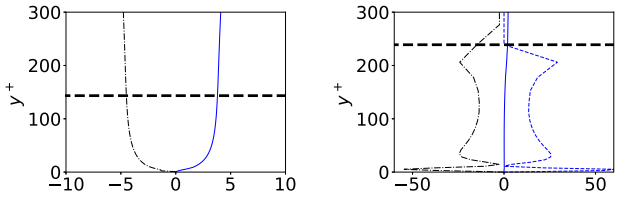

(a) Standard DES. (b) NZ S-DES.

Fig. 7. Channel flow. Forces in the $\langle\bar{u}_1\rangle$ equation (normalized with u_τ^2/δ). Δ_{DES} is used (see Eq. (12)). Thick black dashed line shows the predicted RANS-LES interface. ——: $-\frac{\partial\langle\bar{u}'\bar{v}'\rangle}{\partial x_2}$; – · –: $\frac{\partial}{\partial x_2}\left\langle\left(\nu_{tot}\frac{\partial\bar{u}}{\partial x_2}\right)\right\rangle$; – –: Drift term, S_1^{DES}, see Eq. (6).

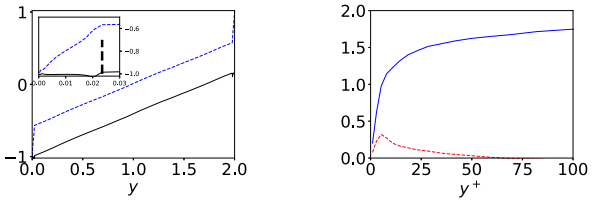

(a) Shear stress, $-\tau^+$, and drift term. – –: total shear stress (Eq. 14); ——: total shear stress plus D (Eq. 15).

(b) Velocity difference between the RANS and DES solvers. ——: $\langle\bar{u}^{RANS}\rangle - \langle\bar{u}^{DES}\rangle$; – –: $\langle\bar{u}^{RANS}/u_\tau^{RANS}\rangle - \langle\bar{u}^{DES}/u_\tau^{DES}\rangle$.

Fig. 8. Channel flow.

the predicted velocities is negligible. In the results presented below, $\hat{T} = 1000$ and $\hat{T} = 1$.

Fig. 5 compares the velocity profiles obtained with NZ S-DES with that of standard DES. The velocity profiles predicted with NZ S-DES agree very well with Reichardt's law whereas the standard DES exhibits the usual log-layer mismatch.

Fig. 6 shows the shear stresses. Fig. 6(b) presents the viscous plus modeled EARSM shear stress in the RANS solver (see inset). As expected, it is much larger than the corresponding term in the DES solver. The location of the interface is furthermore indicated and it can be seen that NZ S-DES puts the interface further away from the wall than the standard DES simulation does (see also Fig. 7). Regarding the resolved shear stresses, we note first that they are zero in the URANS region, see Fig. 6(b). This means that we can maybe not replace the DES solver by a LES solver because the modeled, SGS stress would be too small. This may raise the question if the method is applicable to heat transfer. However, it should be kept in mind that the flow in the URANS region is dictated by the RANS solver and the magnitude of the RANS shear stress is indeed large (see inset in Fig. 6(b)). Second, we find that the magnitude of the resolved shear stress in the LES region is much smaller for NZ S-DES than for standard DES. As a consequence, NZ S-DES also gives a much smaller total shear stress. In fully developed channel flow, the total (resolved, modeled and viscous) shear stress is given by

$$\tau^+_{tot} = \tau^+_w \left(1 - \frac{y}{h}\right). \tag{14}$$

where superscript denotes scaling with u^2_τ. Normally, $\tau^+_w \equiv \rho u^2_\tau = 1$ because the driving pressure gradient is equal to one (the first term on the right side of Eq. (1)). For standard DES (Fig. 6(a)), the stresses and the driving pressure gradient are in balance and as a result the total shear stress varies linearly as dictated by Eq. (14). In NZ S-DES, the wall shear stress, τ^+_w, balances not only the driving pressure gradient but also the drift term. As a result, τ^+_w increases and $\tau^+_{tot} < 1$ at the wall. Xiao et al. (2013) also report that the drift term affects the shear stresses. Fig. 7 presents the forces acting in the streamwise momentum equation, i.e. the gradient of the resolved, modeled and viscous shear stresses, the driving pressure gradient – and for NZ S-DES, see Fig. 7(b) – also the drift term, S^{DES}_1, see Eq. (6). Here we see the effect of the drift term in the DES equations. The drift term drives (increases) – as it should – the time-averaged DES velocity, $\langle \bar{v}_1 \rangle_T$, towards the RANS velocity. The drift term is mainly balanced by the modeled shear stress force (close to the wall it is balanced by the viscous shear stress force). It may be noted that they are very large; the modeled shear stress force is much larger than when using the standard DES (see Fig. 7(a)). It should, however, be recalled that the large drift term is active only in a thin region close to the walls.

Actually, the total shear stress balance equation (Eq. (14)) should include also the integral of the drift term, D, i.e.

$$\tau = \left(u^2_\tau - D\right)\left(1 - \frac{y}{h}\right) \tag{15}$$

so that

$$\tau^+ = \left(1 - \frac{D}{u^2_\tau}\right)\left(1 - \frac{y}{h}\right) \tag{16}$$

where

$$D(y) = \int_0^y S^{DES}_1(\eta) d\eta \tag{17}$$

Fig. 8(a) presents the total shear stress according to Eqs. (14) and (15) and it can be seen when the drift term is included (Eq. (15)), we retrieve $\tau^+_w = 1$ at the lower wall; at the upper wall the total shear stress is equal to $D/u^2_\tau - 1$. Note, that the slope of $-\tau^+$ is not equal to one, but it is given by Eq. (16). The question why the drift term is so large still remains. The drift term (see Eq. (6)) is the product of the difference in the RANS and DES velocities and the inverse of the relaxation time scale, τ_r. Fig. 8(b) presents the velocity differences between the RANS and DES solvers, which are either normalized with u_τ or non-normalized.

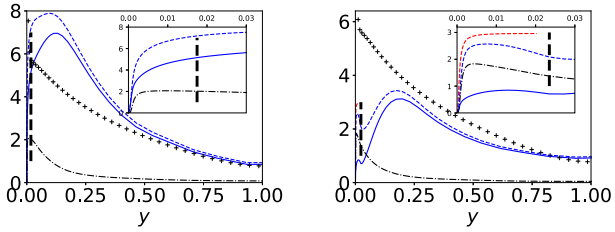

(a) Standard DES. (b) NZ S-DES.

Fig. 9. Channel flow. Streamwise normal stresses scaled with u^2_τ. Δ_{DES} is used (see Eq. (12)). Vertical black dashed lines show predicted RANS-LES interface. ——: resolved; – · –: modeled; ▬ ▬: total. ▬ ▬: modeled in RANS solver (EARSM) in NZ S-DES; ∘: DNS at $Re_\tau = 5200$ (Lee and Moser, 2015).

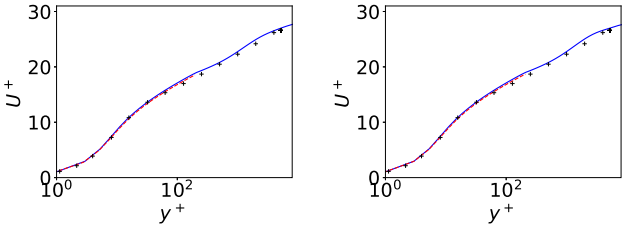

(a) $C_r = 0.02$. (b) $C_r = 0.01$.

Fig. 10. Channel flow. Velocity. Different values of the coefficient, C_r, in the relaxation time (see Eq. (7)). Δ_{DES} is used (see Eq. (12)). ——: DES solver in NZ S-DES; ▬ ▬: RANS solver in NZ S-DES; + : Reichardt's law, $U^+ = \frac{1}{\kappa}\ln(1 - 0.4y^+) + 7.8\left[1 - \exp\left(-y^+/11\right) - (y^+/11)\exp\left(-y^+/3\right)\right]$.

The difference in the normalized velocities is small; this was seen also in Fig. 5. But the difference in the non-normalized velocities is large because the friction velocities predicted by the RANS and DES solvers are different (below we show how this differences decreases as C_r (Eq. (7)) is decreased). This explains the large drift term. Finally, it should be pointed out that the drift term has no physical meaning: its object is simply to make the time-averaged DES velocity match the RANS profile, see Eq. (6). The fact that it is large indicates that it is doing its job.

The streamwise normal stresses are shown in Fig. 9. We find that the resolved stress with NZ S-DES is much smaller than with standard DES. The reason is the drift term (Fig. 7(b)) which balances the eddy-viscosity diffusion force. As a consequence the resolved shear stress force for NZ S-DES is much smaller than for standard DES, see Fig. 7(a). This gives a smaller (absolute) shear stress for NZ S-DES where the drift force is active ($y^+ \lesssim 200$). The small $-\langle \bar{u}'\bar{v}' \rangle$ with NZ S-DES decreases the production term,

$$-\langle \bar{u}'\bar{v}' \rangle \frac{\partial \langle \bar{u} \rangle}{\partial y} \tag{18}$$

in the $\langle \bar{u}'\bar{u}' \rangle$ equation which explains the small $\langle \bar{u}'\bar{u}' \rangle$ in Fig. 9(b). It can also be seen in Fig. 9(b) that the RANS EARSM stress is much larger than the LES eddy-viscosity stress (as expected).

Above we found that the non-normalized velocity difference between the DES and RANS solvers (Fig. 8(b)) is large. Now we will investigate what happens if we decrease the relaxation time, τ_r (see Eqs. (6) and (7)) by decreasing C_r. The baseline value is $C_r = 0.1$. Now we will test $C_r = 0.02$ and $C_r = 0.01$. Figs. 10, 11, 12 and 13 show the streamwise velocity, the shear stress, the force balance and the RANS-DES velocity difference. It is found that a change of the relaxation time by an order of magnitude has very little influence. The largest impact is the decrease in the non-normalized RANS-DES velocity difference as the time scale is decreased (cf. Fig. 8(b)). The drift term does not change which shows that the increase of $1/\tau_r$ is compensated by the decrease in the RANS-DES velocity difference, see Eq. (6).

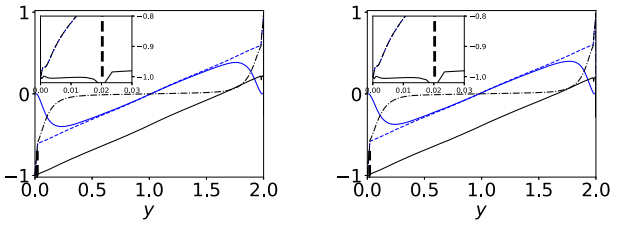

(a) $C_r = 0.02$. (b) $C_r = 0.01$.

Fig. 11. Channel flow. Shear stress, $-\tau^+$, and drift term. Δ_{DES} is used (see Eq. (12)). Different values of the coefficient, C_r, in the relaxation time (see Eq. (7)). — —: total shear stress (Eq. (14)); — · —: viscous + modeled; ——: total shear stress plus D (Eq. (15)).

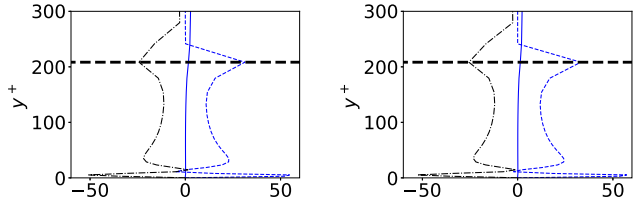

(a) $C_r = 0.02$. (b) $C_r = 0.01$.

Fig. 12. Channel flow. Forces in the $\langle \bar{u}_1 \rangle$ equation (normalized with u_τ^2/δ). Δ_{DES} is used (see Eq. (12)). Thick black dashed line shows the predicted RANS-LES interface. ——: $-\frac{\partial \langle \bar{u}' \bar{v}' \rangle}{\partial x_2}$; — · —: $\frac{\partial}{\partial x_2}\left\langle \left(\nu_{tot} \frac{\partial \bar{u}}{\partial x_2} \right) \right\rangle$; — —: Drift term, S_1^{DES}, see Eq. (6).

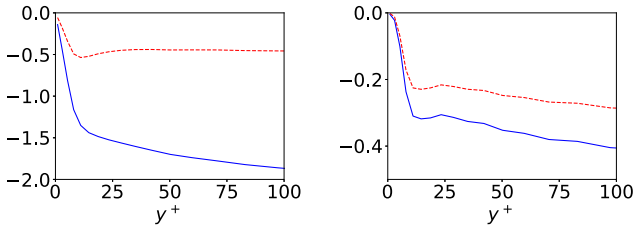

(a) $C_r = 0.02$. (b) $C_r = 0.01$.

Fig. 13. Channel flow. Velocity difference between the RANS and DES solvers. Δ_{DES} is used (see Eq. (12)). ——: $\langle \bar{u}^{RANS} \rangle - \langle \bar{u}^{DES} \rangle$; — —: $\left\langle \bar{u}^{RANS}/u_\tau^{RANS} \right\rangle - \left\langle \bar{u}^{DES}/u_\tau^{DES} \right\rangle$.

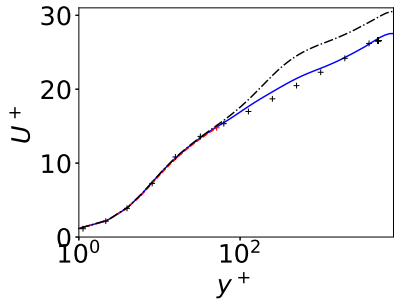

Fig. 14. Channel flow. Δ_{IDDES} is used (see Eq. (12)). NZ S-DES compared with standard DES. ——: DES solver in NZ S-DES; — —: RANS solver in NZ S-DES; — · —: Standard DES; + : Reichardt's law, $U^+ = \frac{1}{\kappa}\ln(1 - 0.4y^+) + 7.8\left[1 - \exp\left(-y^+/11\right) - (y^+/11)\exp\left(-y^+/3\right)\right]$.

The results presented so far were obtained using the DES length scale, Δ_{DES}, see Eq. (12). Next, we present the results where we use the IDDES length scale, Δ_{IDDES}, see Eq. (12). The IDDES length scale is used both for standard DES and NZ S-DES. Fig. 14 presents the velocity profiles. It is seen that NZ S-DES gives much better agreement with

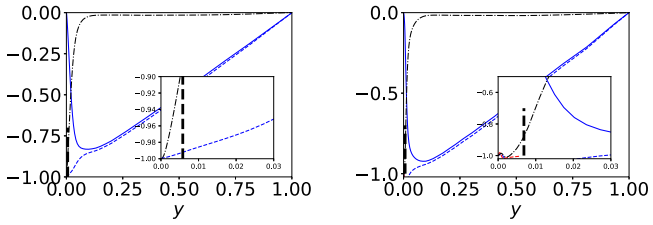

(a) Standard DES. (b) NZ S-DES.

Fig. 15. Channel flow. Shear stresses scaled with u_τ^2. Δ_{IDDES} is used (see Eq. (12)). Vertical black dashed lines show predicted RANS-LES interface. ——: resolved; — · —: viscous + modeled; — —: total.

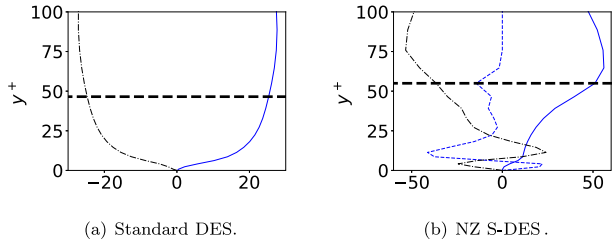

(a) Standard DES. (b) NZ S-DES.

Fig. 16. Channel flow. Forces in the $\langle \bar{u}_1 \rangle$ equation (normalized with u_τ^2/δ). Δ_{IDDES} is used (see Eq. (12)). Thick black dashed line shows the predicted RANS-LES interface. ——: $-\frac{\partial \langle \bar{u}' \bar{v}' \rangle}{\partial x_2}$; — · —: $\frac{\partial}{\partial x_2}\left\langle \left(\nu_{tot} \frac{\partial \bar{u}}{\partial x_2} \right) \right\rangle$; — —: Drift term, S_1^{DES}, see Eq. (6).

the experiments than standard DES which predicts too large a velocity for $y^+ > 100$. Fig. 15 shows the shear stresses. The main difference compared to Fig. 6 (in which Δ_{DES} was used) is that the resolved shear stresses are much larger for both models; the NZ S-DES actually gives a slightly larger shear stress near the wall than standard DES. For NZ S-DES, the predicted total shear stress now closely follows the theoretical linear behavior (which it did not with Δ_{DES}, see Fig. 6(b)); the reason is that the region in which the drift term is active is much smaller. Also, contrary to Fig. 6(b), the resolved fluctuations are not killed in the URANS region; the reason is – again – that the URANS region is much thinner with Δ_{IDDES} than with Δ_{DES}. Another difference – closely related to the large shear stresses – is that, for both models, the RANS-LES interface is located much closer to the wall. This fact reduces the modeled shear stress (since the URANS region is much smaller) and increases the resolved part (since Eq. (14) or (15) must be satisfied). When the RANS-LES interface is moved closer to the wall (compared to Fig. 5), the agreement with experiments deteriorate for standard DES whereas it is not affected for NZ S-DES. This indicates that the NZ S-DES is insensitive to the location of the interface which is a great advantage. Fig. 16 presents the forces in the x direction and it is seen that they are larger than in Fig. 7. The reason is that the gradients of the resolved stresses are larger (and hence also the balancing modeled stresses). One major difference for the $NZS-DES$ model compared to when Δ_{DES} length scale is used, is that the resolved shear stress gives an important contribution in the URANS region; with the Δ_{DES} length scale that contribution is close to zero, see Fig. 7, because the resolved turbulence in the URANS region is close to zero.

Above we have found that changing the relaxation tine, τ_r (Eq. (7)), by an order of magnitude or changing the LES length scale (from Δ_{DES} to Δ_{IDDES}) – which moves the RANS-LES interface from $y^+ \simeq 200$ to $y^+ \simeq 20$ – have very small influence on the performance of NZ S-DES. This is an indication of the robustness of the method. We will now make a final sensitivity check by changing the Reynolds number and changing the RANS turbulence model from EARSM to the $k-\omega$ model. Two additional Reynolds number flows are simulated, one of $Re_\tau = 950$ and one of $Re_\tau = 16\,000$. For $Re_\tau = 16\,000$ the same mesh is used as for $Re_\tau = 8000$. For $Re_\tau = 950$, the number of cells in the y direction is

reduced to 80 and stretching factor of 1.1 is used. Fig. 17(a) presents the streamwise velocity and good agreement is obtained for both Reynolds numbers as well as with the $k-\omega$ model. Fig. 17(b) shows the resolved streamwise fluctuation; they increase with increasing Reynolds number as expected. It may also be noted that the $k-\omega$ in the RANS solver performs at least as good as the EARSM (cf. Fig. 9(b))

4.2. Flat-plate boundary layer

The second test case is developing boundary layer along a flat plate, see Fig. 18. The mean inlet profiles are taken from a 2D RANS solution at $Re_\theta = 6100$. The mesh has $1024 \times 160 \times 64$ cells (x, y, z) with $\Delta t = 0.002$. $\Delta z^+_{in} = 85$ and $\Delta x^+_{in} = 280$. The far-field mean velocity is one, i.e. $U_{free} = 1$. The spanwise extent of the domain is $z_{max} = 2\delta_{in}$. Twice that, i.e. $4\delta_{in}$, has been evaluated which confirms that z_{max} is sufficiently large. Anisotropic synthetic fluctuations are superimposed to the mean inlet velocity profiles. It involves the following steps.

1. A pre-cursor 2D RANS simulation is made using the PDH model (Peng et al., 1997).
2. After having carried out the pre-cursor RANS simulation, the Reynolds stress tensor is computed using the EARSM model (Wallin and Johansson, 2000).
3. The Reynolds stress tensor is used as input for generating the anisotropic synthetic fluctuations. The integral length scale is set to $L_t = 0.3\delta$.
4. Since the method of synthetic turbulence fluctuations assumes homogeneous turbulence, we can only use the Reynolds stress tensor in one point. We need to choose a relevant location for the Reynolds stress tensor. In a turbulent boundary layer, the Reynolds shear stress is by far the most important stress component. Hence, the Reynolds stress tensor is taken at the location where the magnitude of the turbulent shear stress is largest.
5. The synthetic fluctuations are scaled with $\left(|\overline{u'v'}|/|\overline{u'v'}|_{max}\right)^{1/2}_{RANS}$, which is taken from the 2D RANS simulation.
6. Commutation terms in the k and ω equations are used at the inlet (Davidson, 2017; Arvidson et al., 2018).

The only constant we use when generating these synthetic simulations is the prescribed integral length scale which is set to $0.3\delta_{in}$. For more detail, see Davidson (2016), Arvidson et al. (2018). The time, $\mathcal{T}$, to reach fully developed condition and sampling time are both set to $\hat{\mathcal{T}} \equiv \mathcal{T} U_{free}/\delta_{in} = 210$. The averaging time is set to $T = 2$, see Eq. (8).

Fig. 19 presents the skin friction and the mean velocities which are both much better predicted with the NZ S-DES model than the standard DES model. The reason why the standard DES performs that poor is partly found in Fig. 20 which shows the location of the predicted location of the RANS-LES interface which is located close to the wall. It was found also in Deck et al. (2014) that when the interface is located too close to the wall, the standard DES gives poor results. In the channel flow, it was found that – dependent on C_r, see Eq. (7) – there may be a difference between the velocity in the URANS region predicted by the DES and RANS solvers. In this flow, the DES velocity (blue solid lines) and the RANS field (dashed red lines) are very close, see Fig. 19. The streamwise and shear stresses are presented in Figs. 20 and 21. We find that both resolved stresses are much larger for the standard DES than for NZ S-DES. The reason is – as in the channel flow – the drift term, which is shown in Fig. 22(b). The drift term balances the eddy-viscosity diffusion force and as a consequence the resolved shear stress force is much smaller than for standard DES, see Fig. 22(a). This gives a smaller (absolute) shear stress for NZ S-DES – as in the channel flow – where the drift force is active ($y^+ \lesssim 100$). The small $|\langle\bar{u}'\bar{v}'\rangle|$ with NZ S-DES decreases the production term in the $\langle\bar{u}'\bar{u}'\rangle$ equation, see Eq. (18). Finally, it should also be noted that the RANS EARSM stress $\langle\bar{u}'\bar{u}'\rangle$, is – as in the channel flow simulation – much larger than the modeled stress, as expected (see Fig. 20(b)).

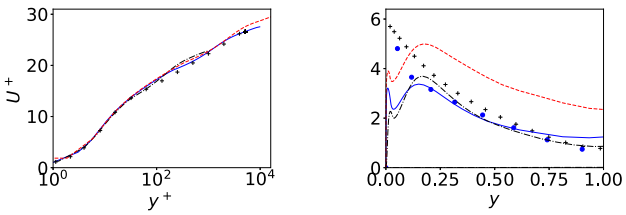

(a) Streamwise velocity. (b) Total streamwise fluctuations. ○: DNS at $Re_\tau = 5\,200$ [20]. ●: DNS at $Re_\tau = 950$ [21].

Fig. 17. Channel flow. ——: $k-\omega$ model in the RANS solver; – –: $Re_\tau = 16\,000$, EARSM; – · –: $Re_\tau = 950$, EARSM.

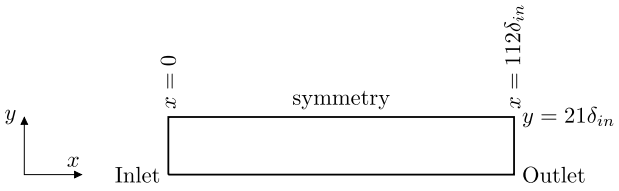

Fig. 18. Boundary layer flow. The domain. $z_{max} = 2.1\delta_{in}$.

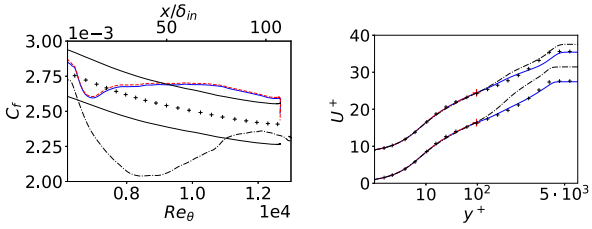

(a) Skinfriction v. momentum thickness. +: expts; ——: ±6%

(b) Mean velocity. Lower lines: $x/\delta_{in} = 37$, $Re_\theta = 8\,000$; upper lines: $x/\delta_{in} = 75$, $Re_\theta = 10\,500$. + DNS at $Re_\theta = 8\,000$.

Fig. 19. Boundary layer flow. Δ_{DES} is used (see Eq. (12)). ——: NZ S-DES; – · –: Standard DES; – –: RANS solver in NZ S-DES.

Now we will investigate the sensitivity to spanwise resolution, a change in relaxation time (Eq. (7)) and RANS turbulence model. The spanwise resolution is coarsened by reducing the number of cells by a factor of two, i.e. $N_k = 32$. The coefficient in the relaxation time is reduced to $C_r = 0.02$. The RANS model is changed from EARSM to $k-\omega$. Fig. 23 presents the skin friction and the streamwise velocity profiles. The small relaxation time scale, $C_r = 0.02$, gives a slightly worse skin friction than the other two cases, but still acceptable. With $C_r = 0.02$, the flow reaches fully developed flow quicker than the other two cases; the reason seems to be smaller resolved turbulence in the initial, developing region. Both the coarse spanwise resolution and the $k-\omega$ model give quite good skin friction. Fig. 24 shows the shear stresses which are quite similar for all three cases. Again, it is noted that the $k-\omega$ model in the RANS solver performs as well as the EARSM. Finally, the forces in the streamwise momentum equation are presented in Fig. 25 for the small relaxation time scale ($N_k = 64$ and $C_r = 0.02$). The drift force is very similar to that for the baseline value $C_r = 0.1$, see Fig. 22.

Next, we change the SGS length scale and instead of Δ_{DES}, we use Δ_{IDDES}, see Eq. (12). Fig. 26 presents the skin friction and the velocity profiles. Both NZ S-DES and the standard DES show a good skin friction, but the standard DES predicts a poor velocity profile. The reason for this poor prediction is found in Fig. 27(b) where we find that the RANS-LES interface is located very close to the wall ($y^+ \simeq 25$). As for the

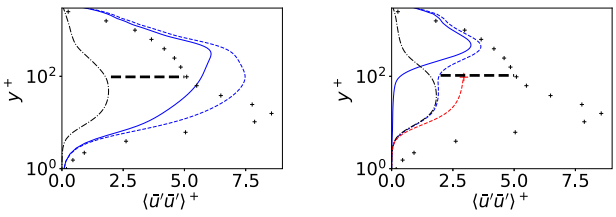

(a) Standard DES (b) NZ S-DES.

Fig. 20. Boundary layer flow. Streamwise normal stresses scaled with u_τ^2. Δ_{DES} is used (see Eq. (12)). $x/\delta_{in} = 75$, $Re_\theta = 10\,500$. + DNS at $Re_\theta = 8000$. ——: resolved; — · —: viscous plus modeled; — —: total; — —: viscous plus modeled in RANS solver (EARSM) in NZ S-DES.

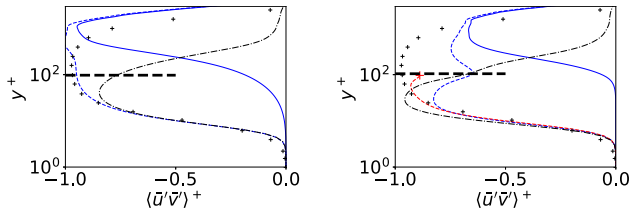

(a) Standard DES (b) NZ S-DES.

Fig. 21. Boundary layer flow. Shear stresses scaled with u_τ^2. Δ_{DES} is used (see Eq. (12)). $x/\delta_{in} = 75$, $Re_\theta = 10\,200$. ——: resolved; — · —: viscous plus modeled; — —: total; — —: viscous plus modeled in RANS solver (EARSM) in NZ S-DES; + DNS at $Re_\theta = 8000$.

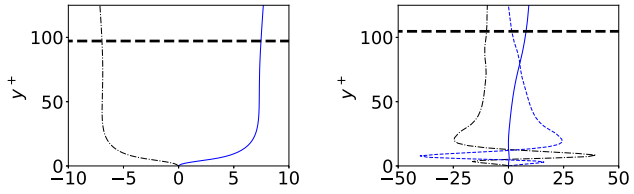

(a) Standard DES. (b) NZ S-DES.

Fig. 22. Boundary layer flow. Forces in the $\langle\bar{u}_1\rangle$ equation (normalized with u_τ^2/δ). $x/\delta_{in} = 75$, $Re_\theta = 10\,500$. Δ_{DES} is used (see Eq. (12)). Thick black dashed line shows the predicted RANS-LES interface. ——: $-\frac{\partial\langle\bar{u}'\bar{v}'\rangle}{\partial x_2}$; — · —: $\frac{\partial}{\partial x_2}\left\langle\left(\nu_{tot}\frac{\partial\bar{u}}{\partial x_2}\right)\right\rangle$; — —: Drift term, S_1^{DES}, see Eq. (6).

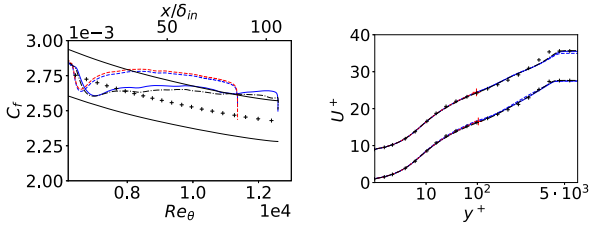

(a) Skinfriction v. momentum thickness. +: expts; ——: ±6%

(b) Mean velocity. Lower lines: $x/\delta_{in} = 37$, $Re_\theta = 8\,000$; upper lines: $x/\delta_{in} = 75$, $Re_\theta = 10\,500$; + DNS at $Re_\theta = 8\,000$.

Fig. 23. Boundary layer flow. Δ_{DES} is used (see Eq. (12)). ——: NZ S-DES, $N_k = 32$; — —: NZ S-DES, $N_k = 64$, $C_r = 0.02$; — · —: $N_k = 32$, $k-\omega$ model in the RANS solver; — —: RANS solver in NZ S-DES $N_k = 64$, $C_r = 0.02$.

channel flow, we find the NZ S-DES is insensitive to the location of the interface. It should be mentioned that the standard DES with the IDDES length scale does give good results if the RANS-LES interface is set at a

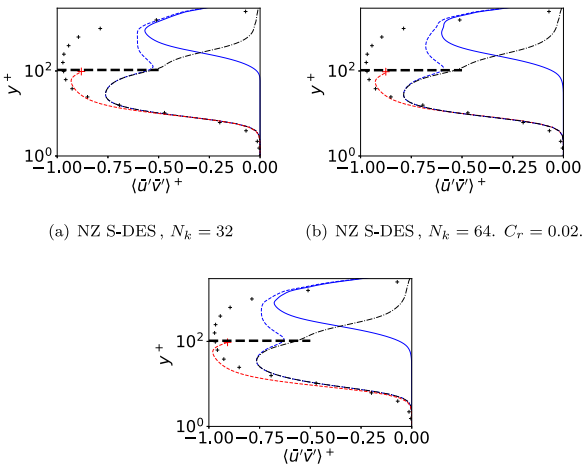

(a) NZ S-DES, $N_k = 32$ (b) NZ S-DES, $N_k = 64$. $C_r = 0.02$.

(c) $N_k = 32$, $k-\omega$ in the RANS solver.

Fig. 24. Boundary layer flow. Shear stresses scaled with u_τ^2. Δ_{DES} is used (see Eq. (12)). $Re_\theta = 10\,200$. ——: resolved; — · —: viscous plus modeled; — —: total; — —: viscous plus modeled in RANS solver (EARSM) in NZ S-DES; + DNS at $Re_\theta = 8000$.

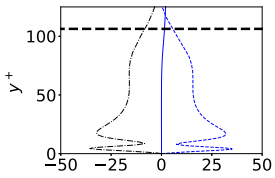

Fig. 25. Boundary layer flow. NZ S-DES, $N_k = 64$, $C_r = 0.02$. Forces in the $\langle\bar{u}_1\rangle$ equation (normalized with u_τ^2/δ). $x/\delta_{in} = 75$, $Re_\theta = 10\,500$. Δ_{DES} is used (see Eq. (12)). Thick black dashed line shows the predicted RANS-LES interface. ——: $-\frac{\partial\langle\bar{u}'\bar{v}'\rangle}{\partial x_2}$; — · —: $\frac{\partial}{\partial x_2}\left(\langle\nu_{tot}\rangle\frac{\partial\langle\bar{u}\rangle}{\partial x_2}\right)$; — —: Drift term, S_1^{DES}, see Eq. (6).

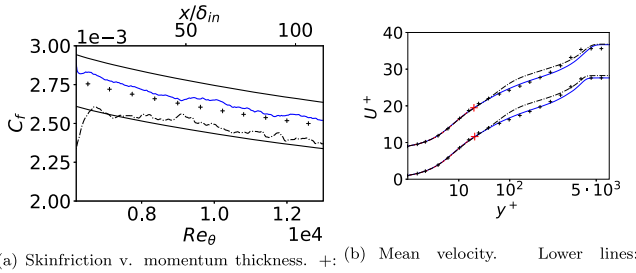

(a) Skinfriction v. momentum thickness. +: expts; ——: ±6%

(b) Mean velocity. Lower lines: $x/\delta_{in} = 37$, $Re_\theta = 8\,000$; upper lines: $x/\delta_{in} = 75$, $Re_\theta = 10\,500$; + DNS at $Re_\theta = 8\,000$.

Fig. 26. Boundary layer flow. Δ_{IDDES} is used (see Eq. (12)). ——: NZ S-DES; — · —: Standard DES; — —: RANS solver in NZ S-DES; + DNS at $Re_\theta = 8000$.

fixed wall-parallel grid line further away from the wall (Arvidson et al., 2018).

Fig. 28(b) presents the shear stress and it is seen that with NZ S-DES – contrary to when Δ_{DES} is used – the resolved shear stresses in the URANS region are not killed. The reason is that the RANS region in which the drift term is active – which dampens resolved fluctuations – is much thinner than with Δ_{DES}. As a result, the resolved shear stress is much larger near the RANS-LES interface.

The forces are shown in Fig. 29 and for NZ S-DES they are found to be much larger than for the case with Δ_{DES} (cf. Fig. 22). The reason is that the interface is located in a region where the modeled stresses are much larger. Although the resolved shear stresses are very large at

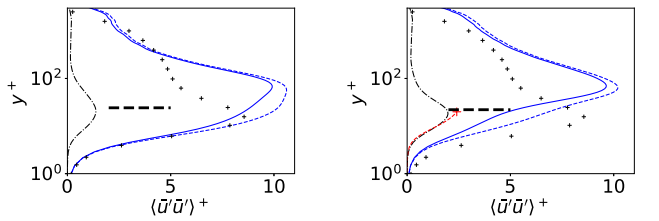

(a) Standard DES (b) NZ S-DES.

Fig. 27. Boundary layer flow. Streamwise normal stresses scaled with u_τ^2. Δ_{IDDES} is used (see Eq. (12)). $x/\delta_{in} = 75$, $Re_\theta = 10\,500$. ——: resolved; — · —: viscous plus modeled; — —: total; — —: viscous plus modeled in RANS solver (EARSM) in NZ S-DES; + DNS at $Re_\theta = 8000$.

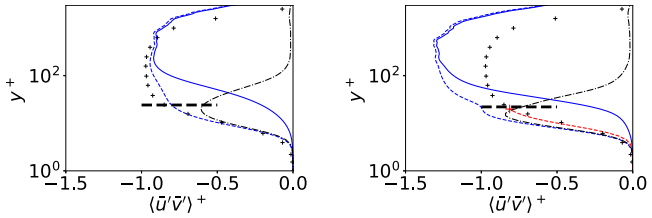

(a) Standard DES (b) NZ S-DES.

Fig. 28. Boundary layer flow. Shear stresses scaled with u_τ^2. Δ_{IDDES} is used (see Eq. (12)). $x/\delta_{in} = 75$, $Re_\theta = 10\,500$. ——: resolved; — · —: viscous plus modeled; — —: total; — —: viscous plus modeled in RANS solver (EARSM) in NZ S-DES; + DNS at $Re_\theta = 8000$.

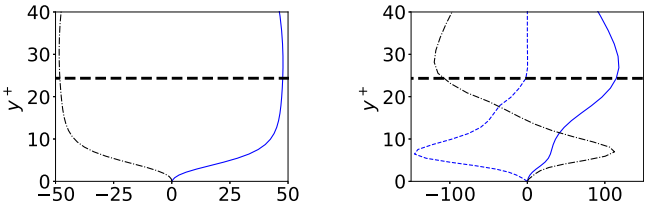

(a) Standard DES. (b) NZ S-DES.

Fig. 29. Boundary layer flow. NZ S-DES. Δ_{IDDES} is used (see Eq. (12)). Forces in the $\langle \bar{u}_1 \rangle$ equation (normalized with u_τ^2/δ). $x/\delta_{in} = 75$, $Re_\theta = 10\,500$. Thick black dashed line shows the predicted RANS-LES interface. ——: $-\frac{\partial \langle \bar{u}'\bar{v}' \rangle}{\partial x_2}$; — · —: $\frac{\partial}{\partial x_2}\left(\langle \nu_{tot} \rangle \frac{\partial \langle \bar{u} \rangle}{\partial x_2}\right)$; — —: Drift term, S_1^{DES}, see Eq. (6).

$y^+ = 20$ in Fig. 29, at $y^+ = 200$ they are actually somewhat smaller (not shown) than those in Fig. 22.

The drift term in NZ S-DES (Fig. 29(b)) is negative (somewhat similar to Fig. 22(b) where it exhibits a negative peak at $y^+ \simeq 10$) and it completely changes the behavior of the modeled diffusion term in the URANS region compared to standard DES (Fig. 29(a)); the modeled diffusion term takes the role of balancing the drift term which makes it positive near the wall whereas it for standard DES is negative (Fig. 29(a))

We have shown that – as for the channel flow – the NZ S-DES is insensitive to location of the RANS-LES interface, spanwise resolution and RANS turbulence model.

4.3. Hump flow

The third test case is the flow over a two-dimensional hump, see Fig. 2. The Reynolds number of the hump flow is $Re_c = 936\,000$, based on the hump length, $c = 1$, and the inlet mean velocity at the centerline, $U_{in,c} = 1$. The inlet is located at $x = -2.1$ and the outlet at $x = 4.0$, see Fig. 2. The mesh has 650 × 110 × 66 cells (x, y, z) and it is based

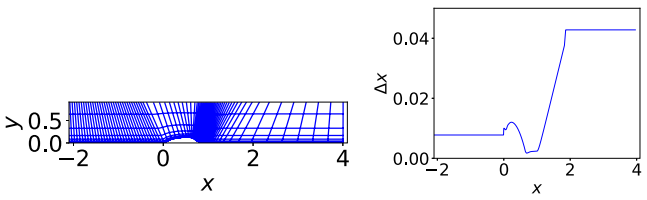

(a) The grid. Every 8^{th} grid line is shown. (b) Streamwise grid spacing near the lower wall.

Fig. 30. Hump flow. Grid and grid spacing.

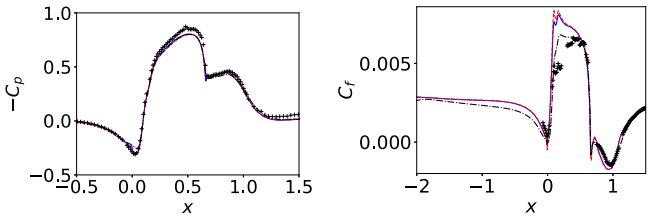

(a) Pressure coefficient. (b) Skinfriction.

Fig. 31. Hump flow. Δ_{DES} is used (see Eq. (12)). ——: NZ S-DES; — · —: standard DES; +: expts (Greenblatt et al., 2004, 2005).

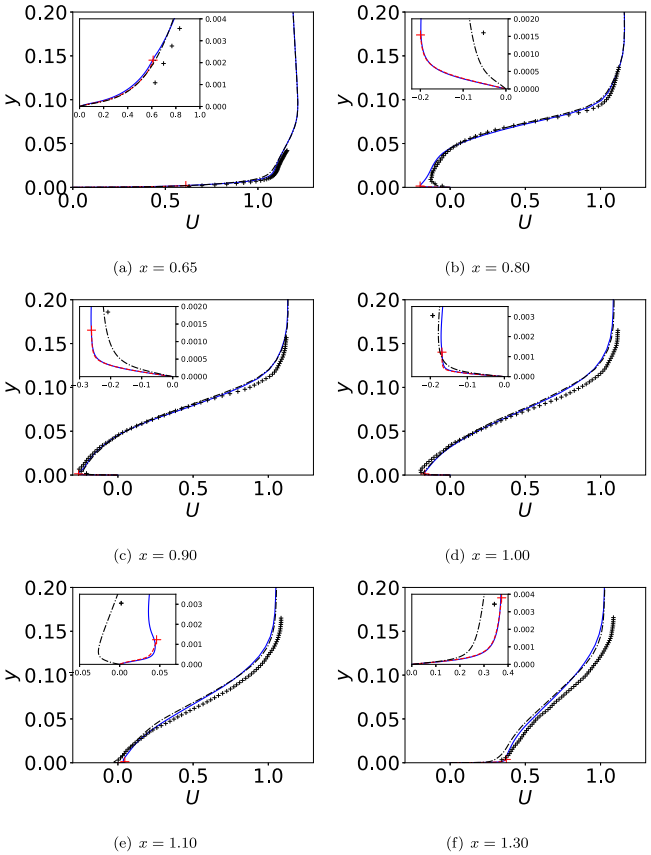

(a) $x = 0.65$ (b) $x = 0.80$ (c) $x = 0.90$ (d) $x = 1.00$ (e) $x = 1.10$ (f) $x = 1.30$

Fig. 32. Hump flow. Velocities. Δ_{DES} is used (see Eq. (12)). +: predicted RANS-LES interface; ——: NZ S-DES, DES solver; — —: NZ S-DES, RANS solver; — · —: standard DES; +: expts (Greenblatt et al., 2004, 2005).

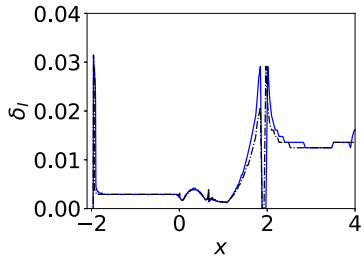

Fig. 33. Hump flow. Δ_{DES} is used (see Eq. (12)). Location of RANS-LES interface, see Fig. 1(b). ——— : NZ S-DES; — · — : standard DES.

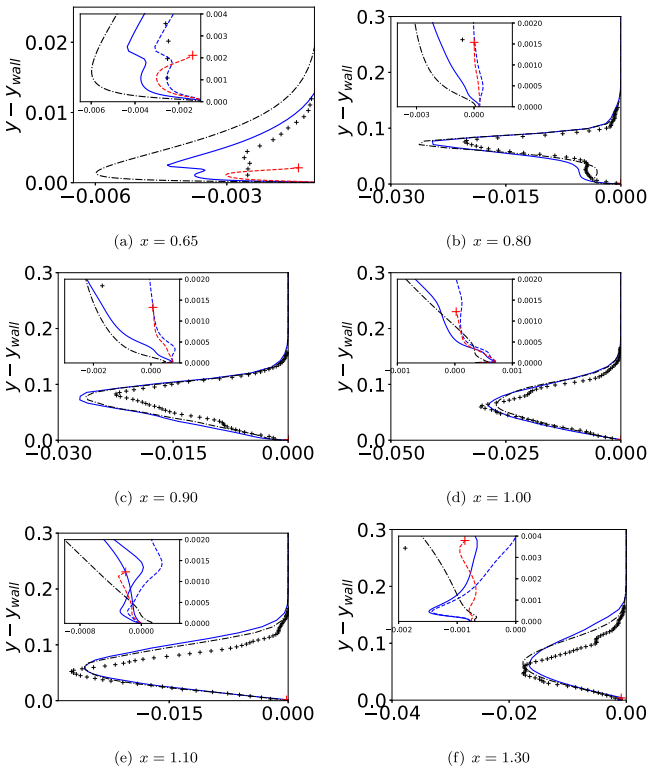

Fig. 34. Hump flow. Total (resolved, modeled and viscous) shear stresses. Δ_{DES} is used (see Eq. (12)). ——— : NZ S-DES, DES solver; + : predicted RANS-LES interface; — — : NZ S-DES, RANS solver (EARSM); — · — : standard DES; + : expts (Greenblatt et al., 2004, 2005).

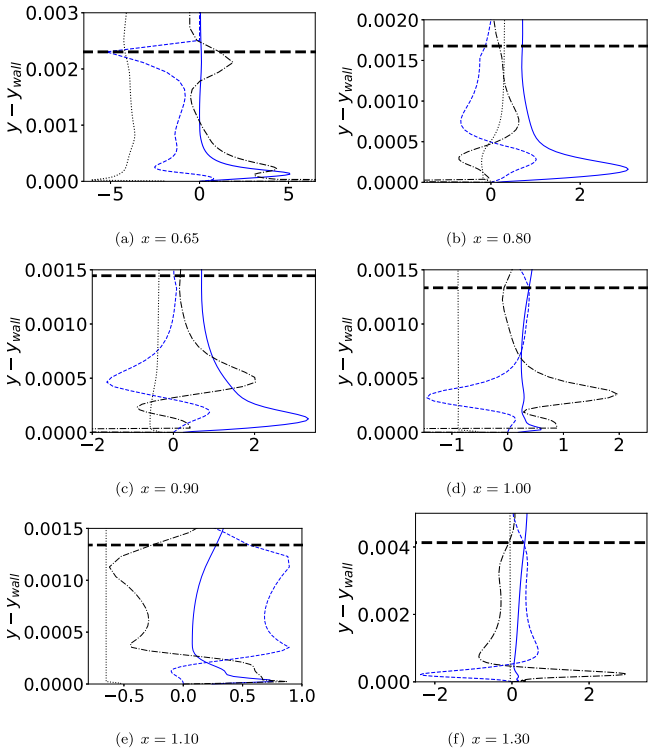

Fig. 35. Hump flow. Forces in the $\langle \bar{u} \rangle$ equation. Δ_{DES} is used (see Eq. (12)). Thick black dashed line shows the predicted RANS-LES interface. ——— : $-\frac{\partial \langle \bar{u}'\bar{v}' \rangle}{\partial y}$; — · — : $\frac{\partial}{\partial y}\left(\langle \nu_{tot} \rangle \frac{\partial \langle \bar{u} \rangle}{\partial y}\right)$; ····· : $-\frac{\partial \langle p \rangle}{\partial x}$; ▬ ▬ : Drift term, S_1^{DES}, see Eq. (6).

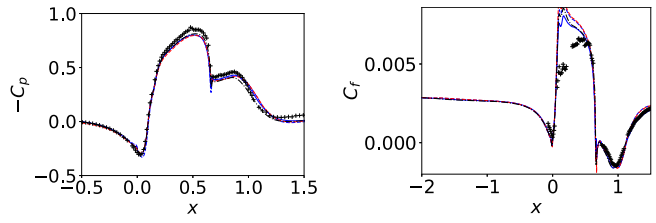

Fig. 36. Hump flow. Δ_{DES} is used (see Eq. (12)). ——— : NZ S-DES, $N_k = 32$; ▬ ▬ : NZ S-DES, $C_r = 0.02$, $N_k = 32$, DES solver; — — : NZ S-DES, $C_r = 0.02$, $N_k = 32$, RANS solver; — · — : $k-\omega$ in the RANS solver; + : expts (Greenblatt et al., 2004, 2005).

on the mesh from the NASA workshop[1] but it is refined upstream of the hump and in the outlet region, see Fig. 30(a). The spanwise extent of the domain is set to 0.3 so that $\Delta z = z_{max}/nk = 0.3/64 = 0.0047$. The required resolution for an LES away from the wall (in the log-region) is $\delta/\Delta x \simeq 10$, $\delta/\Delta z \simeq 20$. The streamwise spacing, Δx, near the wall is shown in Fig. 30(b). The inlet boundary layer thickness is $\delta_{in} = 0.08$ which means that the resolution in the inlet region is reasonable ($\delta_{in}/\Delta x \simeq 10$, $\delta_{in}/\Delta z \simeq 17$). The boundary layer thickness in the recovering region downstream of the reattachment ($x > 2$) is $\delta \simeq 0.13$ (see Fig. 32) so that $\delta/\Delta x \simeq 3$ which is somewhat too small; this region is, however, believed to be less critical than the inlet and hump regions. The time, $\mathcal{T}$, to reach fully developed condition and sampling time are both set to $\hat{\mathcal{T}} \equiv \mathcal{T} U_{free}/h = 100$ (h denotes the height of the hump, see Fig. 2). The averaging time is set to $\hat{T} = 1$, see Eq. (8).

The inlet profiles are taken from a separate 2D RANS simulation with the same momentum thickness as the boundary layer in the experiments (Greenblatt et al., 2004, 2005). Anisotropic synthetic fluctuations are superimposed to the inlet velocity profile in the same way as for the boundary-layer simulations. Periodic boundary conditions are used in the spanwise direction (z). The interface between the URANS and the LES region as well at that between the steady RANS solver and the DES solver is – as in the channel flow and the boundary-layer simulations – defined by Eq. (11). The Δ_{DES} length scale is used, see Eq. (12). The Δ_{IDDES} is not used for this flow since it produces poor results; the reason is most likely that the switch takes place very close to the wall.

The pressure coefficient and skin friction are presented in Fig. 31. As can be seen, the agreement with experiments is good for both NZ S-DES and standard DES. The most obvious discrepancy is the large skin friction predicted by NZ S-DES at $x \simeq 0.17$ and that the standard DES predicts slightly too low a skin friction upstream of the hump (as was also seen for the boundary layer flow, Fig. 19(a)). These two discrepancies are probably connected: the under-predicted skin friction by the standard DES gives a smaller velocity on the upstream part of

[1] https://turbmodels.larc.nasa.gov/nasahump_val.html

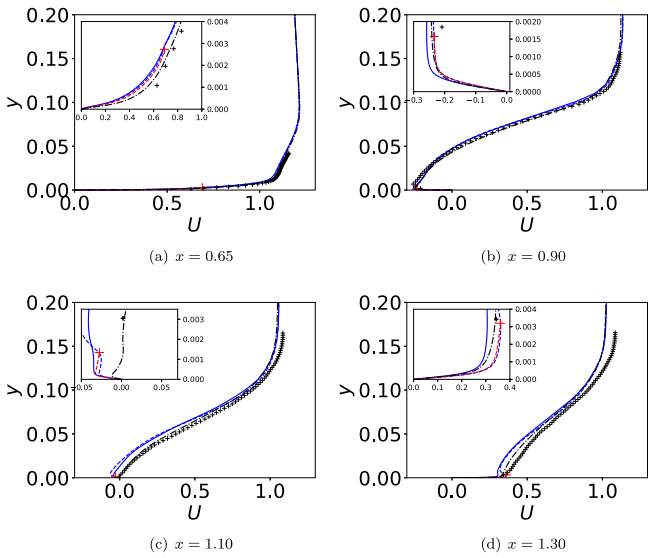

(a) $x = 0.65$ (b) $x = 0.90$

(c) $x = 1.10$ (d) $x = 1.30$

Fig. 37. Hump flow. Velocities. Δ_{DES} is used (see Eq. (12)). ——: NZ S-DES, $N_k = 32$; — —: NZ S-DES, $C_r = 0.02$, $N_k = 32$, DES solver; — —: NZ S-DES, $C_r = 0.02$, $N_k = 32$, RANS solver; — · —: $k-\omega$ in the RANS solver.

the hump and hence a smaller skin friction than NZ S-DES. Hence, the fact that the skin friction is better predicted than NZ S-DES at $x \simeq 0.17$ is probably fortuitous, due to a poor predicted in-coming boundary layer.

Fig. 32 compares the predicted velocity profiles with experiments. The NZ S-DES and standard DES give virtually identical velocity profiles. The NZ S-DES predicts somewhat too strong a backflow (see Fig. 32(b)). The velocity profiles of the RANS solver are also included. The RANS solver velocity profiles in the URANS region match those of the DES solver as they should. The locations of the interface is shown with a red plus sign. It may be noted that the location of the interface at $x = 1.3$ is further away from the wall compared to at $x = 0.65, \ldots, x = 1.1$. This is confirmed in Fig. 33 where the location of the RANS-LES interface is shown. It can be seen that for $x \gtrsim 1.3$, the interface moves away from the wall as x increases. That is because the streamwise grid size is larger in this region, see Fig. 30(b).

Fig. 34 presents the predicted (sum of resolved, modeled and viscous) and measured shear stresses. The agreement between the shear stresses and the measured is good for $x \geq 1.0$. Both NZ S-DES and the standard DES over-predicts the magnitude of the shear stress at $x = 0.65$, but the latter much more; the resolved part of the predicted shear stress with the standard DES is approximately twice as large as the modeled part (not shown). Such large – and even larger – magnitudes of shear stresses at $x = 0.65$ are presented in Garbaruk et al. (2018) where they used the IDDES model. Similar magnitude as in Fig. 34(a) is also seen in Friess and Davidson (2020) using the IDDES and a new IDD-PANS model. It was seen in Fig. 32(b) that the standard DES model predicts an accurate velocity profile, but that is maybe fortuitous and due to incorrect predicted turbulence at $x = 0.65$.

Fig. 35 presents the forces due to resolved and modeled (including viscous) shear stresses and the drift terms. It is seen that the drift term is usually – as for the channel flow and the boundary layer flow – balanced by the modeled shear stresses (the viscous force is negligible except in the vicinity of the wall). Whereas the drift term for the channel flow and the boundary-layer flow is positive – when using Δ_{DES} – it is here both positive and negative. But in the attached region ($x > 1$) it is positive as in the channel flow and the boundary-layer flow.

As for the boundary-layer flow, we make three additional simulations. In one simulation we coarsen the spanwise resolution ($z_{max} = 0.2$, $N_k = 32$), in the second one we replace the EARSM turbulence model by the $k-\omega$ model and in the third one we reduce the relaxation time coefficient to $C_r = 0.02$ (see Eq. (7)). In all cases we use the coarse spanwise resolution ($z_{max} = 0.2$, $N_k = 32$). Figs. 36 and 37 present the pressure coefficient, skin friction and velocity profiles for the three simulations. As can be seen, very good results are obtained. The largest discrepancies are seen in the velocity profiles in the recovery region ($x \geq 1.1$). Actually, the $k-\omega$ model gives the best results. So, once again, it is found that the $k-\omega$ model in the RANS solver gives at least at good results as the EARSM.

5. Conclusions

The paper presents a new non-zonal model based on a steady RANS solver in the URANS region coupled with a DES solver which covers the entire region. The steady RANS solver is called very 10th timestep. It could probably be called less frequently. The RANS solver dictates the flow in the wall region, i.e. the URANS region. A drift term in the URANS region in the DES solver forces the time-averaged DES flow to match that of the RANS flow. This term is often large. It should be stresses that the drift term has no physical meaning. Its only object is to force the time-averaged LES field to agree with the steady RANS field in the URANS region,

The steady RANS solver velocity field is by a large source term forced to be equal to the time-averaged DES flow in the off-wall region, i.e. the LES region. The only object of the steady RANS field in the LES region is to transport the modeled turbulent quantities (k and ω) into the URANS region. They – k and ω – could instead be transported by the time-averaged DES flow.

The new model is evaluated in fully developed channel flow, flat-plate boundary layer and the hump flow. The new model gives very good agreement with experiments. It is found to substantially improve the predicting capability of the standard DES for the channel flow and the boundary layer flow; for the hump flow the two methods give both good agreement with experiments. It is found that the new model is insensitive to the location of the RANS-LES interface which is a great advantage.

Two SGS length scales have been evaluated, Δ_{DES} and Δ_{IDDES}. They both give good results in channel flow and boundary-later flow. With Δ_{IDDES}, the RANS-LES interface is located at $y^+ \simeq 50$ and 20 in the channel and boundary-layer flow, respectively. The corresponding values with Δ_{DES} are 200 and 100. With Δ_{DES} the resolved turbulence with NZ S-DES is in the URANS region close to zero whereas with Δ_{IDDES} the resolved turbulence is substantial. Nevertheless, the NZ S-DES produces very accurate results with both length scales. For the hump flow, however, the Δ_{IDDES} length scale does not give good results (not shown). Hence, we recommend to use the Δ_{DES} length scale in NZ S-DES.

The influence of the relaxation time, τ_r (Eq. (7)), was investigated. It was varied up to a factor of ten in the channel flow and a factor of five in the boundary-layer and the hump flow and it was seen that the variation had negligible effect on the predicted results. Even the magnitude of the drift term was not affected because the increase in $1/\tau_r$ was compensated by a decrease in the difference between the time-averaged LES and the RANS flow fields.

One potential advantage of the present method is that it should pay off to use advanced RANS turbulence models in the RANS solver; the reason is that we solve the steady RANS flow equations for which all RANS turbulence models in the literature have been developed. The explicit algebraic stress model (EARSM) has been used in the present work but it is found that the standard $k-\omega$ model gives at least as good results.

DES is used in present study instead of DDES. The reason is that the author prefer that a large part of the boundary layer should be treated in LES mode. Using DDES would certainly be an option which would be interesting to investigate in future work.

The disadvantage of the present method is of course the complexity it entails to use two solvers and the additional CPU time. Since the

time-averaged flow for all test cases in the present work are two dimensional, a two-dimensional RANS solver was employed and hence the additional CPU time was negligible. In three-dimensional flows, one could consider to use the RANS solver only in the URANS region (maybe solve a simplified set of momentum equations with a prescribed pressure gradient (Bäckar and Davidson, 2017)), and solve the k and ω equations using the time-averaged LES velocities, $\langle \bar{u}_i \rangle_T$, see Eq. (8).

Declaration of competing interest

The authors declare that they have no known competing financial interests or personal relationships that could have appeared to influence the work reported in this paper.

References

Arvidson, S., Davidson, L., Peng, S.-H., 2018. Interface methods for grey-area mitigation in turbulence-resolving hybrid RANS-LES. Int. J. Heat Fluid Flow 73, 236–257.

Bäckar, J.-A., Davidson, L., 2017. Evaluation of numerical wall functions on the axisymmetric impinging jet using OpenFOAM. Int. J. Heat Fluid Flow 67, 27–42.

Breuer, M., Schmidt, S., 2014. Hybrid LES-RANS modeling of complex turbulent flows. Proc. Appl. Math. Mech. 14, 647–650. http://dx.doi.org/10.1002/pamm.201410308.

Davidson, L., 2016. Zonal PANS: evaluation of different treatments of the RANS-LES interface. J. Turbul. 17 (3), 274–307, URL http://dx.doi.org/10.1080/14685248.2015.1093637.

Davidson, L., 2017. Two-equation hybrid RANS-LES models: A novel way to treat k and ω at inlets and at embedded interfaces. J. Turbul. 18 (4), 291–315. http://dx.doi.org/10.1080/14685248.2017.1281417.

Davidson, L., 2018. CALC-LES: A Fortran Code for LES and Hybrid LES-RANS. Tech. Rep., Division of Fluid Dynamics, Dept. of Mechanics and Maritime Sciences, Chalmers University of Technology, Gothenburg.

Davidson, L., 2019a. Zonal Detached Eddy Simulation coupled with steady RANS in the wall region. In: ECCOMAS MSF 2019 Thematic Confernence, Minisyposium "Current Trends in Simulation and Modelling of Turbulent Flows. MS Devoted to 80th Birthday of Prof. Kemo Hanjalic". Sarajevo, Bosnia and Herzegovina.

Davidson, L., 2019b. Non-Zonal Detached Eddy Simulation coupled with a steady RANS solver in the wall region. In: Special Issue on Current Trends in RANS-Based Scale-Resolving Simulation Methods. In: ERCOFTAC Bullentin, vol. 120, pp. 43–48.

Davidson, L., Farhanieh, B., 1995. CALC-BFC: A Finite-Volume Code Employing Collocated Variable Arrangement and Cartesian Velocity Components for Computation of Fluid Flow and Heat Transfer in Complex Three-Dimensional Geometries. Rept. 95/11, Dept. of Thermo and Fluid Dynamics, Chalmers University of Technology, Gothenburg.

Davidson, L., Peng, S.-H., 2003a. Hybrid LES-RANS: A one-equation SGS model combined with a $k-\omega$ for predicting recirculating flows. Internat. J. Numer. Methods Fluids 43 (9), 1003–1018.

Davidson, L., Peng, S.-H., 2003b. Hybrid LES-RANS: A one-equation SGS Model combined with a $k-\omega$ model for predicting recirculating flows. Internat. J. Numer. Methods Fluids 43, 1003–1018.

de Laage de Meux, B., Audebert, B., Manceau, R., Perrin, R., 2015. Anisotropic linear forcing for synthetic turbulence generation in large eddy simulation and hybrid RANS/LES modeling. Phys. Fluids A 27, 035115.

Deck, S., Renard, N., Laraufie, R., Sagaut, P., 2014. Zonal detached eddy simulation (ZDES) of a spatially eveloping flat plate turbulent boundary layer over the Reynolds number range $3\,150 \leq Re_\theta \leq 14\,000$. Phys. Fluids A 26, 025116.

Emvin, P., 1997. The Full Multigrid Method Applied to Turbulent Flow in Ventilated Enclosures Using Structured and Unstructured Grids (Ph.D. thesis). Dept. of Thermo and Fluid Dynamics, Chalmers University of Technology, Göteborg.

Friess, C., Davidson, L., 2020. A formulation of PANS able to mimic IDDES. Int. J. Heat Fluid Flow 86, 108666, URL https://doi.org/10.1016/j.ijheatfluidflow.2020.108666.

Garbaruk, A., Guseva, E., Shur, M., Strelets, M., Travin, A., 2018. 2D wall-mounted hump. In: Mockett, C., Haase, W., Schwamborn, D. (Eds.), Go4Hybrid: Grey Area Mitigation for Hybrid RANS-LES Methods. In: Notes on Numerical Fluid Mechanics and Multidisciplinary Design, vol. 134, Springer Verlag, pp. 173–188.

Greenblatt, D., Paschal, K.B., Yao, C.-S., Harris, J., 2005. A separation control CFD validation test case Part 1: Zero efflux oscillatory blowing. In: 43rd AIAA Aerospace Sciences Meeting and Exhibit, Reno, NV. AIAA-2005-0485.

Greenblatt, D., Paschal, K.B., Yao, C.-S., Harris, J., Schaeffler, N.W., Washburn, A.E., 2004. A separation control CFD validation test case. Part 1: Baseline & steady suction. In: 2nd AIAA Flow Control Conference, Portland, OR. AIAA-2004-2220.

Lee, M., Moser, R.D., 2015. Direct numerical simulation of turbulent channel flow up to $Re_\tau \approx 5200$. J. Fluid Mech. 774, 395–415. http://dx.doi.org/10.1017/jfm.2015.268.

Meneveau, C., Lund, T., Cabot, W., 1996. A lagrangian dynamic model subgrid-scale model of turbulence. J. Fluid Mech. 315, 353–385.

Nguyen, P., Uribe, J., Afgan, I., Laurence, D., 2020. A dual-grid hybrid RANS/LES model for under-resolved near-wall regions and its application to heated and separating flows. Flow Turbul. Combust. 104, 835–859, URL https://doi.org/10.1007/s10494-019-00070-8.

Patankar, S.V., 1980. Numerical Heat Transfer and Fluid Flow. McGraw-Hill, New York.

Peng, S.-H., Davidson, L., Holmberg, S., 1997. A modified low-reynolds-number $k-\omega$ model for recirculating flows. J. Fluids Eng. 119, 867–875.

Schumann, U., 1975. Subgrid scale model for finite difference simulations of turbulent flows in plane channels and annuli. J. Comput. Phys. 18 (4), 376–404. http://dx.doi.org/10.1016/0021-9991(75)90093-5.

Shur, M.L., Spalart, P.R., Strelets, M.K., Travin, A.K., 2008. A hybrid RANS-LES approach with delayed-DES and wall-modelled LES capabilities. Int. J. Heat Fluid Flow 29, 1638–1649, URL https://doi.org/10.1016/j.ijheatfluidflow.2008.07.001.

Spalart, P.R., Jou, W.-H., Strelets, M., Allmaras, S.R., 1997. Comments on the feasability of LES for wings and on a hybrid RANS/LES approach. In: Liu, C., Liu, Z. (Eds.), Advances in LES/DNS, First Int. Conf. on DNS/LES. Greyden Press, Louisiana Tech University.

Tunstall, R., Laurence, D., Prosser, R., Skillen, A., 2017. Towards a generalised dual-mesh hybrid LES/RANS framework with improved consistency. Comput. & Fluids 157, 73–83.

van Leer, B., 1979. Towards the ultimate conservative difference scheme. V. A second-order sequel to godonov's method. J. Comput. Phys. 32, 101–136.

Wallin, S., Johansson, A.V., 2000. A new explicit algebraic reynolds stress model for incompressible and compressible turbulent flows. J. Fluid Mech. 403, 89–132.

Xiao, H., Jenny, P., 2012. A consistent dual-mesh framework for hybrid LES/RANS modeling. J. Comput. Phys. 231, 1848–1865.

Xiao, H., Sakai, Y., Henniger, R., Wild, M., Jenny, P., 2013. Coupling of solvers with non-conforming computational domains in a dual-mesh hybrid LES/RANS framework. Comput. & Fluids 88, 653–662.